galaxies

MDPI

Article

Expectations for Horizon-Scale Supermassive Black Hole Population Studies with the ngEHT

Dominic W. Pesce [1,2,*], Daniel C. M. Palumbo [1,2], Angelo Ricarte [1,2], Avery E. Broderick [3,4,5], Michael D. Johnson [1,2], Neil M. Nagar [6], Priyamvada Natarajan [2,7,8] and José L. Gómez [9]

1 Center for Astrophysics | Harvard & Smithsonian, 60 Garden Street, Cambridge, MA 02138, USA
2 Black Hole Initiative, Harvard University, 20 Garden Street, Cambridge, MA 02138, USA
3 Perimeter Institute for Theoretical Physics, 31 Caroline Street North, Waterloo, ON N2L 2Y5, Canada
4 Department of Physics and Astronomy, University of Waterloo, 200 University Avenue West, Waterloo, ON N2L 3G1, Canada
5 Waterloo Centre for Astrophysics, University of Waterloo, Waterloo, ON N2L 3G1, Canada
6 Astronomy Department, Universidad de Concepción, Casilla 160-C, Concepción 4030000, Chile
7 Department of Astronomy, Yale University, 52 Hillhouse Avenue, New Haven, CT 06511, USA
8 Department of Physics, Yale University, P.O. Box 208121, New Haven, CT 06520, USA
9 Instituto de Astrofísica de Andalucía-CíSIC, Glorieta de la Astronomía s/n, E-18008 Granada, Spain
* Correspondence: dpesce@cfa.harvard.edu

Abstract: We present estimates for the number of supermassive black holes (SMBHs) for which the next-generation Event Horizon Telescope (ngEHT) can identify the black hole "shadow", along with estimates for how many black hole masses and spins the ngEHT can expect to constrain using measurements of horizon-resolved emission structure. Building on prior theoretical studies of SMBH accretion flows and analyses carried out by the Event Horizon Telescope (EHT) collaboration, we construct a simple geometric model for the polarized emission structure around a black hole, and we associate parameters of this model with the three physical quantities of interest. We generate a large number of realistic synthetic ngEHT datasets across different assumed source sizes and flux densities, and we estimate the precision with which our defined proxies for physical parameters could be measured from these datasets. Under April weather conditions and using an observing frequency of 230 GHz, we predict that a "Phase 1" ngEHT can potentially measure ∼50 black hole masses, ∼30 black hole spins, and ∼7 black hole shadows across the entire sky.

Keywords: SMBHs; VLBI; ngEHT

check for updates

Citation: Pesce, D.W.; Palumbo, D.C.M.; Ricarte, A.; Broderick, A.E.; Johnson, M.D.; Nagar, N.M.; Natarajan, P.; Gómez, J.L. Expectations for Horizon-Scale Supermassive Black Hole Population Studies with the ngEHT. *Galaxies* **2022**, *10*, 109. https://doi.org/10.3390/galaxies10060109

Academic Editor: Luigina Feretti

Received: 6 November 2022
Accepted: 25 November 2022
Published: 2 December 2022

1. Introduction

The Event Horizon Telescope (EHT) observations of the supermassive black holes (SMBHs) in M87 [1–8] and Sgr A* [9–14] are the first in a new era of horizon-scale studies of black holes. The primary observational signature on horizon scales is the black hole "shadow", a ring-like emission structure surrounding a darker central region [15,16]. Simulations of accretion flows around SMBHs generically produce images that exhibit such shadows [5,13], which typically have a size comparable to that of the theoretical curve bounding the locus of impact parameters for photon trajectories that escape the black hole (i.e., the "apparent shape" of the black hole, from Bardeen [17]). A driving motivation for the EHT to pursue observations of M87* and Sgr A* was because these sources were anticipated to have the largest shadow sizes of all black holes on the sky [1].

The next-generation Event Horizon Telescope (ngEHT) will build on the capabilities of the EHT by improving (u, v)-coverage through the addition of more stations to the array, increasing baseline sensitivities by using wider observing bandwidths, and accessing finer angular resolution by observing at higher frequencies [18]. A natural question to ask is whether these improved capabilities will yield access to a larger pool of shadow-resolved

SMBHs. The horizon-scale emission structure around a black hole encodes spacetime properties such as its mass and spin, and the detection of a shadow is a distinct and relatively unambiguous identifier of the observed object's black hole nature. Access to a population of shadow-resolved SMBHs would thus provide an opportunity to make uniquely direct and self-consistent measurements of such spacetime properties, with attendant implications for studies of SMBH formation, growth, and co-evolution with host galaxies.

The suitability of any particular SMBH for shadow-resolving ngEHT observations depends primarily on three properties [19]:

1. the angular size of the SMBH shadow (θ);
2. the total horizon-scale flux density emitted by the source (S_ν); and
3. the optical depth of the emitting material.

The first of the above properties is set primarily by the mass of and distance to the black hole, while the latter two are more complex and depend also on the mass accretion rate and other physical conditions in the accretion flow. However, the detectability of horizon-scale structure from a SMBH does not guarantee the measurability of any particular quantity of interest; additional conditions must be met to ensure that, e.g., a black hole mass can be measured, or that the ring-like structure associated with the black hole shadow can be distinguished from other possible emission morphologies.

In this paper, we provide estimates for the number of SMBHs for which the ngEHT could plausibly make mass, spin, and shadow measurements. In Section 2, we define observational proxies for each of these quantities of interest that can be accessed from the horizon-scale emission structure. Section 3 describes our synthetic data generation procedure and our approach to estimating parameter measurement precision from ngEHT data. Our conditions for the measurability of each proxy are defined in Section 4, where we also report the number of objects expected to satisfy these conditions for each quantity of interest. We summarize and conclude in Section 5. Throughout this paper, we use the results from Pesce et al. [19] as our baseline for how many SMBHs satisfy the above three detection criteria as a function of θ and S_ν.[1]

2. Measurable Proxies for Quantities of Interest

For a given SMBH, the two primary quantities of scientific interest are its mass and spin, neither of which is directly observable by the ngEHT. Instead, analyses of ngEHT observations will need to identify and measure features of the emission structure that serve as proxies for the desired quantities, or else they will need to carry out some form of physical modeling to infer the SMBH mass and/or spin from the ngEHT data. For the proof-of-concept analyses presented in this paper, we pursue the former strategy.

2.1. Proxy for SMBH Shadows

One of the most generic predictions from simulated images of SMBHs is that the observed emission structure on event horizon scales should exhibit a ring-like morphology associated with the black hole shadow (e.g., [5,13]). Though it is possible for other processes to give rise to ring-like emission structures—e.g., the Einstein ring from a bright, compact emitter passing behind the black hole—in such cases the ring-like structure is expected to be transient. For the purposes of this paper, we thus consider the observation of a ring-like emission morphology to be a proxy for verifying the object's black hole nature. If we can determine from ngEHT observations that the emission structure from a particular object is ring-like—i.e., if we can discern the shadow—then we can identify that object as a black hole.

2.2. Proxy for SMBH Masses

The mass of a SMBH sets the physical scale for its associated spacetime metric, and all spacetime-sensitive length scales in the system should thus exhibit a proportionality with the gravitational radius,

$$\theta_g = \frac{GM}{c^2 D}, \tag{1}$$

with M the black hole mass and D its distance from Earth. The most observationally accessible length scale is the overall size of the emission region, which for a ring-like emission structure corresponds to the ring diameter, d. The EHT has demonstrated that black hole mass measurements for both M87* and Sgr A* can be made by calibrating the scaling relationship between d and θ_g using a large number of simulated images of the emission structure [6,12]. In this paper, we thus take d to be a proxy for M^2; i.e., we assume that if d can be measured for a particular SMBH, then M can also be determined.

2.3. Proxy for SMBH Spins

The spin, a, of a SMBH has historically proven to be more difficult to measure than the mass; e.g., the EHT observations of M87* and Sgr A* have not yet yielded strong constraints on the spin of either SMBH [5,13]. There are a number of possible avenues for measuring a from horizon-scale images of SMBH systems (e.g., [23]), but the most observationally accessible of these approaches target the imprint of the SMBH spin on the horizon-scale magnetic field topology, which in turn can be accessed through observations of the linear polarization structure around the ring (e.g., [7,8]). Palumbo et al. [24] have developed a useful decomposition of the polarization structure in terms of a basis that captures the azimuthal behavior of the electric vector position angle (EVPA, i.e., the orientation of the linear polarization around the ring). This decomposition takes the form

$$\beta_m = \frac{1}{S_0} \iint P(r,\phi) e^{-im\phi} r \mathrm{d}r \mathrm{d}\phi, \tag{2}$$

where (r,ϕ) are polar coordinates in the image, $P(r,\phi) = Q(r,\phi) + iU(r,\phi)$ is the complex-valued linear polarization field (with Q and U the standard Stokes intensities), and S_0 is a flux normalization factor. When studying images of M87* from GRMHD simulations, Palumbo et al. [24] found that the "twisted" morphology of the linear polarization pattern, quantified by the (complex-valued) β_2 coefficient, is correlated with the spin of the black hole. It is now believed that this relation arises from a magnetic field geometry that evolves with the black hole spin: black holes with larger spins exhibit more frame dragging, and produce more strongly toroidal magnetic fields than lower-spin black holes [25]. Qiu et al. [26] further explored the connection between polarized image morphology and SMBH spin, finding that the asymmetry (A) of the Stokes I emission, the polarimetric β_1 mode, and the modulus of the polarimetric β_2 mode also encode spin information (though β_2 continues to stand out as the most discriminating measurable parameter). In this paper, we thus take a joint measurement of β_1, β_2, and A to be our proxy for a.

3. Synthetic Data Generation and Fitting Procedure

To determine the region of the (θ, S_ν) parameter space—and thus the number of SMBHs—for which the quantities of interest described in the previous section could be measured by the ngEHT, we carry out a series of model-fitting exercises using synthetic data. We use a model for the SMBH emission structure that captures the salient features relevant for measuring the physical quantities of interest. Per Section 2, these salient features include the diameter and thickness of the emitting ring, as well as the structure of the linear polarization pattern. As our parameterization of the SMBH emission structure, we thus use a polarized "m-ring" model [12,27] convolved with a circular Gaussian blurring kernel. This model is restricted to describing ring-like morphologies, but it can flexibly distribute both the total intensity and the linearly polarized flux about the ring using a relatively small number of parameters. The emission structures produced by this model qualitatively match those expected from both simple analytic treatments (e.g., [28]) as well as numerical GRMHD simulations (e.g., [8,12]).

In our polarized source model, the Stokes I image structure is given by

$$I(r,\phi) = \left[\frac{S_0}{\pi d} \delta\left(r - \frac{d}{2}\right) \sum_{k=-m}^{m} \alpha_k e^{ik\phi} \right] * \left[\frac{4\ln(2)}{\pi W^2} \exp\left(-\frac{4\ln(2) r^2}{W^2} \right) \right], \tag{3}$$

where $*$ denotes the convolution operation, d is the ring diameter, W is the FWHM ring width, and δ denotes the Dirac delta function. We enforce $\alpha_0 = 1$ so that S_0 is the total flux density, and we also enforce $\alpha_{-k} = \alpha_k^*$ so that the image intensity is real-valued. We define $A = |\alpha_1|$ to be the asymmetry parameter mentioned in Section 2 as potentially relevant for spin constraints.[3] The linear polarization structure is similarly given by

$$P(r,\phi) = \left[\frac{1}{\pi d} \delta\left(r - \frac{d}{2}\right) \sum_{k=-m}^{m} \beta_k e^{ik\phi} \right] * \left[\frac{4\ln(2)}{\pi W^2} \exp\left(-\frac{4\ln(2) r^2}{W^2} \right) \right], \tag{4}$$

where we now allow both β_{-k} and β_k to be free parameters because P is complex-valued in general.

We generate a number of synthetic SMBH images by gridding the (d, S_0) parameter space, spanning $[0.1, 100]$ μas in d and $[10^{-3}, 1]$ Jy in S_0, with both dimensions uniformly gridded on a logarithmic scale. We set $m = 1$ for the Stokes I emission, with both the real and imaginary parts of α_1 uniformly sampled within $[-0.5, 0.5]$. For the polarized emission we set $m = 2$, with the real and imaginary parts of β_0 and β_{-2} uniformly sampled within $[-0.1, 0.1]$, the real and imaginary parts of β_1 and β_{-1} uniformly sampled within $[-0.05, 0.05]$, and the real and imaginary parts of β_2 uniformly sampled within $[-0.3, 0.3]$. For all synthetic images, we enforce $W = d/3$. Though these choices are not unique, they cover a range of parameter values similar to that seen in the GRMHD simulations developed by the EHT collaboration [5,13]. An example polarized m-ring image generated using these specifications is shown in Figure 1.

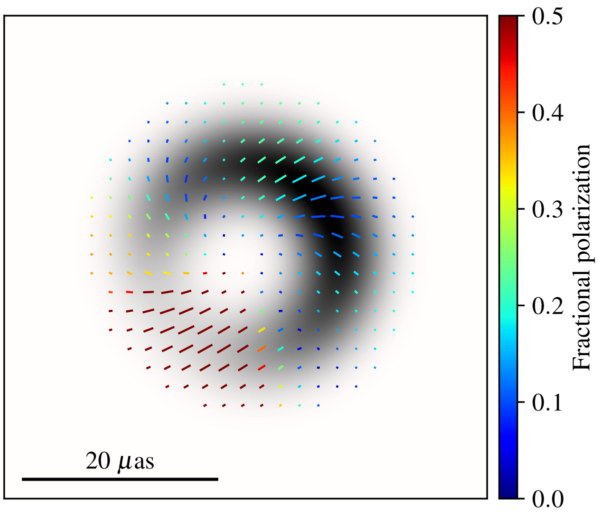

Figure 1. Example polarized source model used for generating the synthetic data described in Section 3. The grayscale image shows the Stokes I emission, while the colored ticks mark the EVPA of the linear polarization structure. The length of each tick is proportional to the intensity of the linear polarization (i.e., $|P|$), while the color of each tick reflects the fractional polarization (i.e., $|P|/I$).

To generate synthetic ngEHT observations corresponding to the synthetic images, we use the `ngehtsim`[4] package, which expands on the synthetic data generating functionality of the `ehtim` library [30,31]. We assume the observations are carried out at an observing frequency of 230 GHz and with 8 GHz of bandwidth using the "full" ngEHT Phase 1 array configuration from [32], which consists of the 2022 EHT array plus the OVRO 10.4 m dish, the Haystack 37 m dish, and three 6.1 m dishes located in Baja California (Mexico), Las Campanas Observatory (Chile), and the Canary Islands (Spain). We use historical weather data to determine appropriate system equivalent flux densities at each site following a procedure similar to that in Raymond et al. [33]. To emulate fringe-finding signal-to-noise ratio (SNR) thresholds, we flag any visibilities from baselines that contain a station not participating in at least one other baseline that achieves an SNR of 5 in a 10-s integration time. We add complex station gain corruptions at the level of 10% in amplitude and uniformly sampled within $[0, 2\pi]$ in phase for all stations on every 300-s time interval, to emulate scans, and we assume that the data have been calibrated to remove polarimetric leakage effects.

We generate synthetic datasets across a grid in right ascension and declination, with spacings between grid points of 1 h in right ascension and 10 degrees in declination. To gather information on the performance of the array in different weather conditions and for different black hole structure realizations, we generate 100 instantiations of synthetic data at each grid location. We assume weather conditions typical for the month of April.

For each synthetic dataset, we estimate the precision with which the parameters of a polarized m-ring model fit to the data could be recovered. We compute these estimates using a Fisher matrix approach implemented within the `ngEHTforecast`[5] package. This approach does not explicitly carry out fits of the model to the data; instead, it assumes that a "good" fit to the data has already been achieved, and it then provides an estimate of the uncertainty in each of the fitted parameters via a second-order expansion of the logarithmic probability density around the best-fit location. We compute parameter precision estimates assuming that the fits have been carried out using complex visibilities as the input data products, with broad priors on the station gain amplitudes and phases at every scan.

4. Results: The Expected Number of Measurable SMBH Masses, Spins, and Shadows

The results of the modeling exercises described in the previous section are summarized in Figure 2, which shows the sky density of sources expected to have measurable masses (top panel), spins (middle panel), and shadows (bottom panel). At each sky location, the plotted density corresponds to an average over 100 instantiations of weather conditions and source structure. Our criteria for determining whether a particular mass, spin, or shadow is deemed "measurable" are as follows:

1. Our condition for whether a SMBH has a measurable mass is that the fractional uncertainty in the measurement of the ring diameter d must be at the level of 20% or lower (i.e., it is measured with a statistical significance $\gtrsim 5\sigma$). Values of (θ, S_ν) for which this condition is satisfied fall to the upper right of the red dashed curve in Figure 3.
2. Our condition for whether a SMBH has a measurable spin is that the uncertainty in the measurement of all spin-relevant parameters (as determined by Qiu et al. [26]; see also Section 2.3) must be at the level of 20% or lower. Specifically, we require the fractional uncertainty in $|\alpha_1|$, $|\beta_1|$, and $|\beta_2|$ and the uncertainty in $\arg(\beta_1)$ and $\arg(\beta_2)$ to all be less than 0.2 (i.e., 20%). Values of (θ, S_ν) for which this condition is satisfied fall to the upper right of the green dashed curve in Figure 3.
3. Our condition for whether a SMBH has a measurable shadow is that the fractional width W/d deviates from unity with an uncertainty of 20% or smaller; i.e., we require that $W < d$ with a statistical significance $\gtrsim 5\sigma$. Values of (θ, S_ν) for which this condition is satisfied fall to the upper right of the blue dashed curve in Figure 3.

Given the above measurability thresholds, we can see from Figure 3 that there is a hierarchy of measurement difficulty with increasing S_ν and θ. The "easiest" quantity to measure is d (and thus the black hole mass), which can be recovered for $\sim$50 sources after integrating over the whole sky. The next most well-constrained quantities are those pertaining to the black hole spin, which we find can be recovered for ∼30 sources. The most difficult quantity to measure is W (and thus the black hole shadow), which can be recovered for ∼7 sources. The measurements are cumulative within this hierarchy: for all sources for which spin is measurable, mass is also measurable; for all sources for which the shadow is measurable, both spin and mass are also measurable.

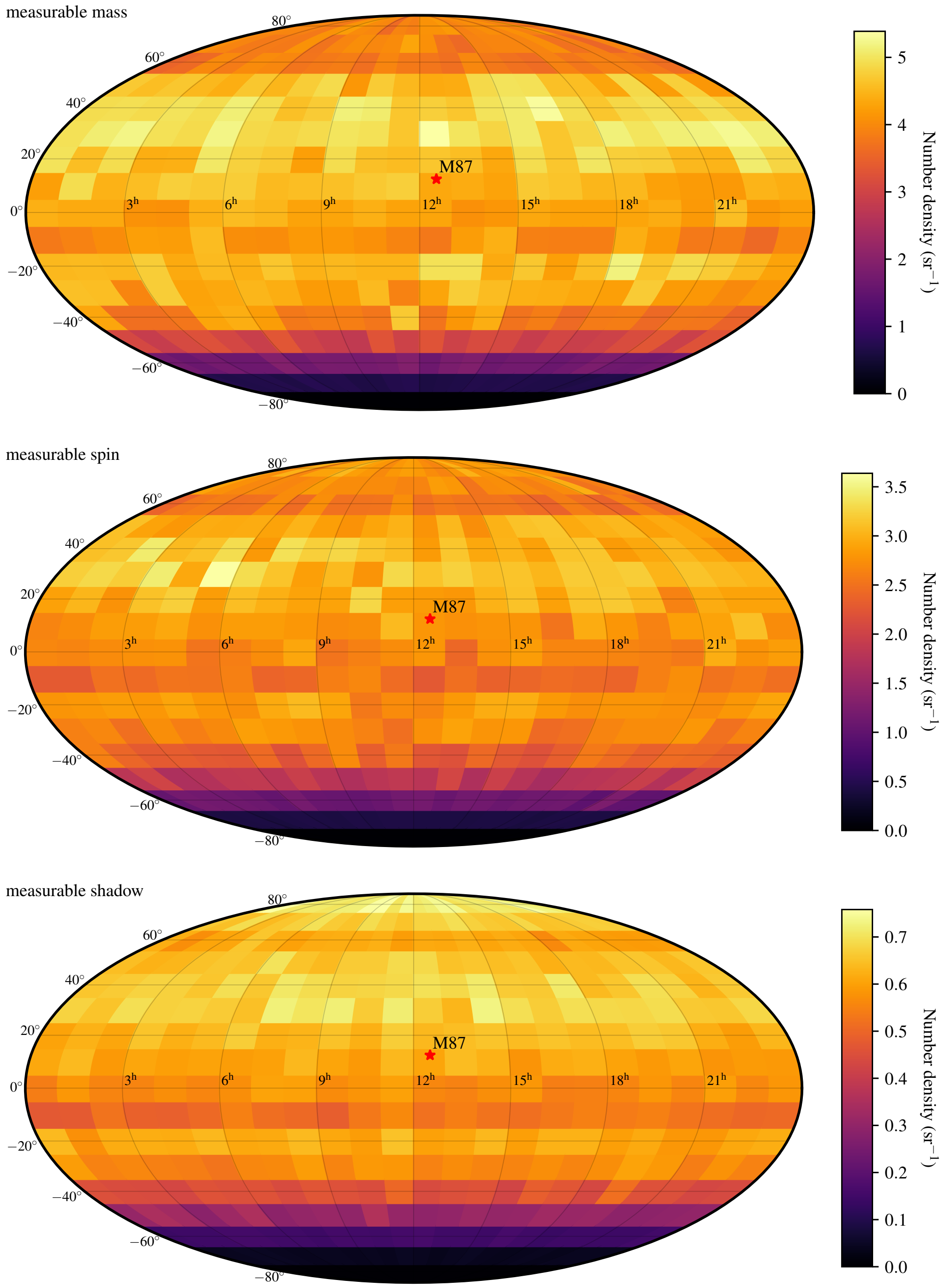

Figure 2. Estimated sky density of SMBHs with measurable masses (top), spins (middle), and shadows (bottom), as a function of right ascension and declination. These estimates have been determined according to the criteria outlined in Section 4, and they assume an underlying distribution of observable SMBHs from Pesce et al. [19]. The stochastic variations seen from pixel to pixel are primarily the result of sampling noise. The location of M87* is marked with a red star.

All three quantities of interest exhibit two regimes of non-measurability in Figure 3. For sources with flux densities below $S_\nu \lesssim 10\,\text{mJy}$, the source is too weak to be detected on most baselines, and there are thus simply insufficient data to enable significant constraints on the parameters of interest. For sources that are stronger than $\sim$10 mJy but smaller than several μas, there can be many detected data points, but the source is insufficiently resolved to enable significant constraints on morphological parameters. In both regimes, all three quantities of interest exhibit a measurability tradeoff between θ and S_ν. In the second regime, this tradeoff is such that it is possible to make a measurement for sources with smaller θ so long as they have sufficiently larger S_ν (because increasing signal-to-noise ratio permits subtler features to be recovered), while in the first regime the tradeoff is reversed (because compact sources yield more detections—particularly on long baselines—than extended sources).

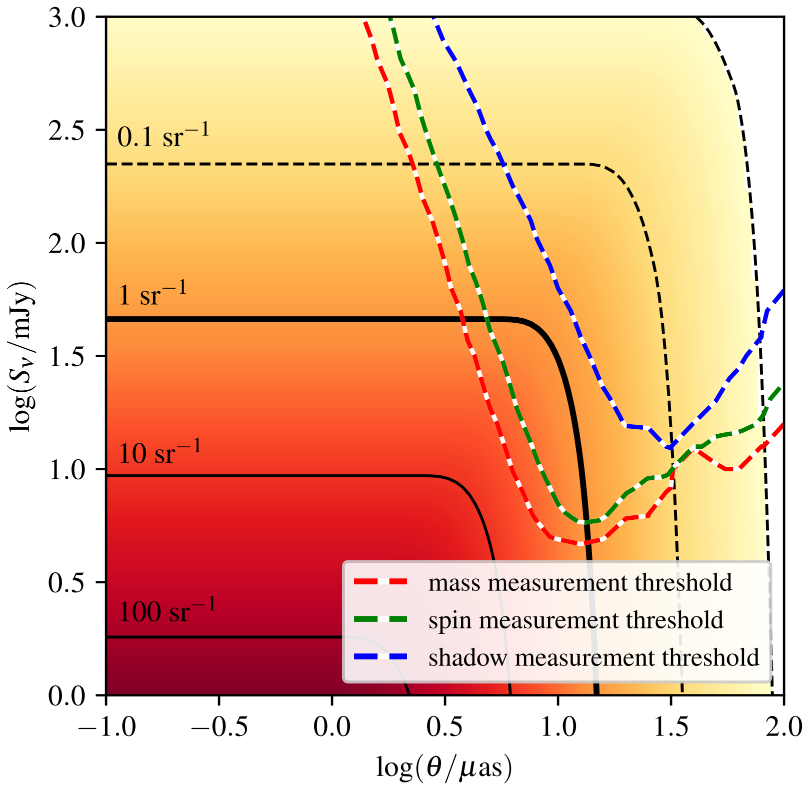

Figure 3. Approximate number density of SMBHs that are expected to satisfy different thresholds of measurability, assuming an observing frequency of 230 GHz. The background colorscale and contours mark the number density (per unit solid angle) of SMBHs that have flux densities greater than S_ν and shadow diameters larger than θ, as a function of S_ν and θ and assuming that sources are distributed isotropically on the sky [19]. The solid contours start with the thick contour indicating a count of 1 and then increase by factors of 10 towards the lower left, while the dashed contours each decrease by a factor of ten towards the upper right. The overplotted colored dashed contours indicate where various parameters of interest could be measurable for different combinations of (θ, S_ν), assuming observations appropriate for the "full" ngEHT Phase 1 array observing at a declination of 10 degrees (i.e., averaged over right ascension). The red dashed contour marks the lower boundary of the region in which black hole mass can be measured, the green dashed contour marks the lower boundary of the region in which black hole spin can be measured, and the blue dashed contour marks the lower boundary of the region in which black hole shadow can be measured.

Figure 2 shows the sky distribution of objects with measurable masses, spins, and shadows, after averaging over weather and source structure instantiations. We find that the distribution is quite uniform, and that accessible objects can be located almost anywhere in the sky; there is no strong dependence on right ascension. The only major gaps in accessibility are for sources having declinations within ∼30 degrees of the southern celestial pole, for which the (u, v)-coverage of the array is particularly poor. A modest increase in source density is seen around declinations of ∼30–40 degrees, where the (u, v)-coverage of the array is densest. For the shadow measurements, we also see a modest increase in source density around the northern celestial pole; northern polar observations provide the most complete long-baseline coverage, so this bump in density may indicate that the long baselines are the most constraining for the width parameter.

5. Summary and Conclusions

To date, the EHT has observed the horizon-scale emission structure around two SMBHs. The ngEHT aims to improve on the capabilities of the EHT by adding new dishes to the array, increasing the observing bandwidth, and expanding the frequency coverage, all of which will improve the sensitivity and fidelity of reconstructed images.

Motivated by the promise of the ngEHT for population studies of SMBHs, we have identified three scientific quantities of interest that the ngEHT can expect to measure for a number of SMBHs: the black hole mass, the black hole spin, and the black hole shadow. We construct a geometric ring model for the polarized emission structure around a SMBH, and we identify parameters of this model as observable proxies for the scientific quantities of interest. Specifically, we associate the diameter of the ring with measurements of the black hole mass, the thickness of the ring with measurements of the black hole shadow, and the linear polarization structure with measurements of the black hole spin.

Assuming a Phase 1 ngEHT array configuration observing in April conditions at a frequency of 230 GHz, we generate a large number of realistic synthetic observations spanning a range of source structure (i.e., flux density S_ν and angular size θ) and site weather (i.e., opacity and atmospheric temperature) instantiations. For each synthetic dataset, we use a Fisher matrix formalism to estimate the precision with which each of the geometric ring model parameters of interest could be measured. We use the statistics of these measurement precision estimates (across all weather instantiations) to determine the corresponding number of SMBHs on the sky whose properties could be well-constrained as a function of S_ν and θ. We carry out this procedure for synthetic observations covering a grid in right ascension and declination, finding that the sky density of measurable sources (in each parameter of interest) is approximately uniform for declinations above roughly -60°.

Associating these measurable parameters with their corresponding physical quantities of interest, we present estimates for the number of SMBHs for which the Phase 1 ngEHT can expect to make measurements of these quantities. Integrating over the whole sky, we find that the Phase 1 ngEHT should be able to measure ∼50 black hole masses, ∼30 black hole spins, and ∼7 black hole shadows. The measurable SMBHs have characteristic observed flux densities of ∼30 mJy and angular sizes of ∼10 μas; per Pesce et al. [19], we expect the bulk of these SMBHs to lie in the redshift range between $z \approx 0.01$ and $z \approx 0.1$. Our estimate for the number of measurable shadows is consistent with the predictions from Pesce et al. [19].

We note that our detection criteria for mass and spin are likely optimistic. A primary analysis limitation is that our model for the appearance of an SMBH does not include emission that extends much beyond the near-horizon region. Mass estimates for SMBHs of interest to the ngEHT may be complicated by additional image features—such as, e.g., AGN jets (e.g., [34]—that could limit the ability to accurately estimate the ring diameter when it is only marginally resolved or weakly detected. For spin, the situation is even more uncertain: the EHT has already produced tight estimates for the ring parameters β_1, β_2, and A for M87*, but it has not yet claimed a corresponding measurement of the black hole spin [6–8]. A secure association between these ring parameters and spin will require a combination of continued observational and theoretical studies.

On the other hand, we have employed a simplified analysis that likely underestimates the number of accessible sources, given any particular set of detection criteria. For instance, the synthetic datasets used in this paper are currently limited to April weather conditions and an observing frequency of 230 GHz; a more comprehensive exploration of year-round weather conditions and the addition of a 345 GHz observing band would likely increase the number of accessible sources. Furthermore, the synthetic datasets generated for the analyses in this paper have assumed an EHT-like calibration procedure; more advanced calibration strategies that can bootstrap phase information across frequency bands (e.g., [35]) are also expected to increase the number of accessible sources. Addressing these shortcomings will be the focus of future work.

Observationally, the most critical next step is to identify a list of credible targets and start surveying them to determine flux densities and compactness for ngEHT followup. Ramakrishnan et al. [36] are compiling a comprehensive sample of all plausible ngEHT AGN targets, which is expected serve as a source catalog for pursuing SMBH population studies with the ngEHT.

Author Contributions: Conceptualization, J.L.G., P.N., D.W.P.; methodology, M.D.J., D.C.M.P., D.W.P., A.R.; software, A.E.B., M.D.J., D.W.P.; writing—original draft preparation, D.W.P.; writing—review and editing, A.E.B., J.L.G., M.D.J., N.M.N., P.N., D.C.M.P., D.W.P., A.R.; visualization, D.W.P.; supervision, J.L.G., P.N. All authors have read and agreed to the published version of the manuscript.

Funding: Support for this work was provided by the NSF through grants AST-1440254, AST-1935980, and AST-2034306, and by the Gordon and Betty Moore Foundation through grant GBMF-10423. This work has been supported in part by the Black Hole Initiative at Harvard University, which is funded by grants from the John Templeton Foundation and the Gordon and Betty Moore Foundation to Harvard University. NN acknowledges funding from TITANs NCN19-058 and Fondecyt 1221421.

Conflicts of Interest: The authors declare no conflict of interest.

Notes

1. The procedure Pesce et al. [19] used to determine the number of observable SMBHs involves integrating the supermassive black hole mass function (BHMF) to determine how many objects have shadow diameters larger than θ, while also using a semi-analytic spectral energy distribution model and adopting an empirically motivated prescription for the SMBH Eddington ratio distribution function to restrict the objects under consideration to those that have flux densities greater than S_ν and accretion flows that are optically thin. The distribution of sources used in this paper assumes an observing frequency of 230 GHz and a BHMF determined using the stellar mass function from Behroozi et al. [20] scaled according to the relation determined by Kormendy and Ho [21] (i.e., the "upper BHMF" from Pesce et al. [19]).
2. We note that the spin of a black hole also has an effect on the shadow size, but the impact of spin is small ($\sim$4%; Takahashi [22]) and is dominated by the $\gtrsim$10% systematic uncertainty associated with the unknown accretion flow morphology [6,12]).
3. Note that this definition for A differs from that in Qiu et al. [26], who instead adopt the asymmetry definition used in Medeiros et al. [29].
4. https://github.com/Smithsonian/ngehtsim, accessed on 5 November 2022.
5. https://github.com/aeb/ngEHTforecast, accessed on 5 November 2022.

References

1. Akiyama, K. et al. [Event Horizon Telescope Collaboration] First M87 Event Horizon Telescope Results. I. The Shadow of the Supermassive Black Hole. *Astrophys. J. Lett.* **2019**, *875*, L1.
2. Akiyama, K. et al. [Event Horizon Telescope Collaboration] First M87 Event Horizon Telescope Results. II. Array and Instrumentation. *Astrophys. J. Lett.* **2019**, *875*, L2.
3. Akiyama, K. et al. [Event Horizon Telescope Collaboration] First M87 Event Horizon Telescope Results. III. Data Processing and Calibration. *Astrophys. J. Lett.* **2019**, *875*, L3.
4. Akiyama, K. et al. [Event Horizon Telescope Collaboration] First M87 Event Horizon Telescope Results. IV. Imaging the Central Supermassive Black Hole. *Astrophys. J. Lett.* **2019**, *875*, L4.
5. Akiyama, K. et al. [Event Horizon Telescope Collaboration] First M87 Event Horizon Telescope Results. V. Physical Origin of the Asymmetric Ring. *Astrophys. J. Lett.* **2019**, *875*, L5.
6. Akiyama, K. et al. [Event Horizon Telescope Collaboration] First M87 Event Horizon Telescope Results. VI. The Shadow and Mass of the Central Black Hole. *Astrophys. J. Lett.* **2019**, *875*, L6.

7. Akiyama, K. et al. [Event Horizon Telescope Collaboration] First M87 Event Horizon Telescope Results. VII. Polarization of the Ring. *Astrophys. J. Lett.* **2021**, *910*, L12.
8. Event Horizon Telescope Collaboration.; Akiyama, K.; Algaba, J.C.; Alberdi, A.; Alef, W.; Anantua, R.; Asada, K.; Azulay, R.; Baczko, A.K.; Ball, D.; et al. First M87 Event Horizon Telescope Results. VIII. Magnetic Field Structure near The Event Horizon. *Astrophys. J. Lett.* **2021**, *910*, L13.
9. Akiyama, K. et al. [Event Horizon Telescope Collaboration] First Sagittarius A* Event Horizon Telescope Results. I. The Shadow of the Supermassive Black Hole in the Center of the Milky Way. *Astrophys. J. Lett.* **2022**, *930*, L12. [CrossRef]
10. Akiyama, K. et al. [Event Horizon Telescope Collaboration] First Sagittarius A* Event Horizon Telescope Results. II. EHT and Multiwavelength Observations, Data Processing, and Calibration. *Astrophys. J. Lett.* **2022**, *930*, L13. [CrossRef]
11. Akiyama, K. et al. [Event Horizon Telescope Collaboration] First Sagittarius A* Event Horizon Telescope Results. III. Imaging of the Galactic Center Supermassive Black Hole. *Astrophys. J. Lett.* **2022**, *930*, L14. [CrossRef]
12. Akiyama, K. et al. [Event Horizon Telescope Collaboration] First Sagittarius A* Event Horizon Telescope Results. IV. Variability, Morphology, and Black Hole Mass. *Astrophys. J. Lett.* **2022**, *930*, L15. [CrossRef]
13. Akiyama, K. et al. [Event Horizon Telescope Collaboration] First Sagittarius A* Event Horizon Telescope Results. V. Testing Astrophysical Models of the Galactic Center Black Hole. *Astrophys. J. Lett.* **2022**, *930*, L16. [CrossRef]
14. Akiyama, K. et al. [Event Horizon Telescope Collaboration] First Sagittarius A* Event Horizon Telescope Results. VI. Testing the Black Hole Metric. *Astrophys. J. Lett.* **2022**, *930*, L17. [CrossRef]
15. Falcke, H.; Melia, F.; Agol, E. Viewing the Shadow of the Black Hole at the Galactic Center. *Astrophys. J. Lett.* **2000**, *528*, L13–L16.
16. Narayan, R.; Johnson, M.D.; Gammie, C.F. The Shadow of a Spherically Accreting Black Hole. *Astrophys. J. Lett.* **2019**, *885*, L33.
17. Bardeen, J.M. Timelike and null geodesics in the Kerr metric. In *Proceedings of the Black Holes (Les Astres Occlus)*; Gordon and Breach: New York, NY, USA, 1973; pp. 215–239.
18. Doeleman, S.; Blackburn, L.; Dexter, J.; Gomez, J.L.; Johnson, M.D.; Palumbo, D.C.; Weintroub, J.; Farah, J.R.; Fish, V.; Loinard, L.; et al. Studying Black Holes on Horizon Scales with VLBI Ground Arrays. *Bull. Am. Astron. Soc.* **2019**, *51*, 256.
19. Pesce, D.W.; Palumbo, D.C.M.; Narayan, R.; Blackburn, L.; Doeleman, S.S.; Johnson, M.D.; Ma, C.P.; Nagar, N.M.; Natarajan, P.; Ricarte, A. Toward Determining the Number of Observable Supermassive Black Hole Shadows. *Astrophys. J.* **2021**, *923*, 260.
20. Behroozi, P.; Wechsler, R.H.; Hearin, A.P.; Conroy, C. UNIVERSEMACHINE: The correlation between galaxy growth and dark matter halo assembly from z = 0-10. *Mon. Not. R. Astron. Soc.* **2019**, *488*, 3143–3194.
21. Kormendy, J.; Ho, L.C. Coevolution (Or Not) of Supermassive Black Holes and Host Galaxies. *Annu. Rev. Astron. Astrophys.* **2013**, *51*, 511–653.
22. Takahashi, R. Shapes and Positions of Black Hole Shadows in Accretion Disks and Spin Parameters of Black Holes. *Astrophys. J.* **2004**, *611*, 996–1004.
23. Ricarte, A.; Tiede, P.; Emami, R.; Tamar, A.; Natarajan, P. The ngEHT's Role in Measuring Supermassive Black Hole Spins. *arXiv* **2022**, arXiv:2211.03910.
24. Palumbo, D.C.M.; Wong, G.N.; Prather, B.S. Discriminating Accretion States via Rotational Symmetry in Simulated Polarimetric Images of M87. *Astrophys. J.* **2020**, *894*, 156.
25. Emami, R.; Ricarte, A.; Wong, G.N.; Palumbo, D.; Chang, D.; Doeleman, S.S.; Broaderick, A.; Narayan, R.; Weintroub, J.; Wielgus, M.; et al. Unraveling Twisty Linear Polarization Morphologies in Black Hole Images. *arXiv* **2022**, arXiv:2210.01218.
26. Qiu, R.; Ricarte, A.; Narayan, R.; Wong, G.N.; Chael, A.; Palumbo, D.C.M. Using Machine Learning to Link Black Hole Accretion Flows with Spatially Resolved Polarimetric Observables. 2022, *in preparation*.
27. Johnson, M.D.; Lupsasca, A.; Strominger, A.; Wong, G.N.; Hadar, S.; Kapec, D.; Narayan, R.; Chael, A.; Gammie, C.F.; Galison, P.; et al. Universal interferometric signatures of a black hole's photon ring. *Sci. Adv.* **2020**, *6*, eaaz1310.
28. Gelles, Z.; Himwich, E.; Johnson, M.D.; Palumbo, D.C.M. Polarized image of equatorial emission in the Kerr geometry. *Phys. Rev. D* **2021**, *104*, 044060.
29. Medeiros, L.; Chan, C.K.; Narayan, R.; Özel, F.; Psaltis, D. Brightness Asymmetry of Black Hole Images as a Probe of Observer Inclination. *Astrophys. J.* **2022**, *924*, 46,
30. Chael, A.A.; Johnson, M.D.; Narayan, R.; Doeleman, S.S.; Wardle, J.F.C.; Bouman, K.L. High-resolution Linear Polarimetric Imaging for the Event Horizon Telescope. *Astrophys. J.* **2016**, *829*, 11,
31. Chael, A.A.; Johnson, M.D.; Bouman, K.L.; Blackburn, L.L.; Akiyama, K.; Narayan, R. Interferometric Imaging Directly with Closure Phases and Closure Amplitudes. *Astrophys. J.* **2018**, *857*, 23.
32. Doeleman, S.S. et al. [Event Horizon Telescope Collaboration] Reference Array and Design Consideration for the next-generation Event Horizon Telescope. 2022. *in preparation*.
33. Raymond, A.W.; Palumbo, D.; Paine, S.N.; Blackburn, L.; Córdova Rosado, R.; Doeleman, S.S.; Farah, J.R.; Johnson, M.D.; Roelofs, F.; Tilanus, R.P.J.; et al. Evaluation of New Submillimeter VLBI Sites for the Event Horizon Telescope. *Astrophys. J.* **2021**, *253*, 5.
34. Janssen, M.; Falcke, H.; Kadler, M.; Ros, E.; Wielgus, M.; Akiyama, K.; Baloković, M.; Blackburn, L.; Bouman, K.L.; Chael, A.; et al. Event Horizon Telescope observations of the jet launching and collimation in Centaurus A. *Nat. Astron.* **2021**, *5*, 1017–1028.
35. Rioja, M.J.; Dodson, R. Precise radio astrometry and new developments for the next-generation of instruments. *Astron. Astrophys. Rev.* **2020**, *28*, 6.
36. Ramakrishnan, V. et al. [Event Horizon Telescope Collaboration] ETHER. 2022. *in preparation*.